Terrigenous Sedimentation on the Submarine Shirshov Ridge (Bering Sea) during the Last Deglaciation

I. O. Murdmaa[a, *], E. V. Dorokhova[a, **], E. A. Ovsepyan[a, *], O. M. Dara[a], and D. Nürnberg[b]**

[a]Shirshov Institute of Oceanology, Russian Academy of Sciences Nakhimovskii pr. 36, Moscow, 117997 Russia
[b]GEOMAR, Helmholtz Center for Ocean Research Kiel, Wischhofstrasse 1-3, D-24148 Kiel, Germany
*e-mail: murdmaa@mail.ru
**e-mail: zhdorokhova@gmail.com
***e-mail: eovsepyan@ocean.ru

Abstract—The submarine Shirshov Ridge is an independent system of terrigenous sedimentation, which is geomorphologically isolated from bottom terrigenous influx into the deep-water basin of the Bering Sea. Using the ridge as example, we studied background hemipelagic sedimentation of the finely dispersed terrigenous suspended matter from water column and deposition of the coarser grained ice-rafted material in the western part of the deep-water basin. Both the grain-size and mineral composition of postglacial sediments of the Shirshov Ridge were studied in cores SO201-2-85KL and SO201-2-77KL taken in local basins in the central and southern parts of the ridge, respectively. Statistic processing of uninterrupted grain-size distributions (GD) of terrigenous component of the postglacial sediments by end-member (EM) modeling revealed that the grain-size composition of sediments from two cores is determined by the mixing of three EMs. EM-1 and EM-2 reflect the hemipelagic sedimentation with and without bottom currents, respectively, while EM-3 with mode at fine-grained sand characterizes GD of the ice-rafted material. Reconstructed mechanisms of terrigenous influx on the Shirshov Ridge involve advection of the suspended matter with surface and intermediate water masses and ice-rafting. The relative role of both mechanisms of terrigenous sedimentation is evaluated. The conditions of the varying bottom current velocities are taken into account for intervals of Last Glacial Maximum, early deglaciation, Heinrich event 1, Bølling–Allerød, Younger Dryas, and Early Holocene. It is established that the grain-size composition of terrigenous component is controlled by climatic variations, sea ice coverage, drift pathways, conditions of fast sea ice melting, and mobility of bottom waters. High concentrations of drifting ice or permanent sea ice cover likely existed above the southern part of the ridge during the second half of the Heinrich 1 event. The low mobility of bottom waters facilitated only the subice hemipelagic sedimentation of fine fractions from the background reserve of suspended matter. A sharp reduction of ice-rafted flux was reconstructed for the Bølling–Allerød warming interval. Bottom currents affected sedimentation in the central part of the ridge during the entire deglaciation (in addition to the second half of the Heinrich 1 event), and in the southern part during the Bølling–Allerød, Younger Dryas, and Early Holocene.

INTRODUCTION

The study of postglacial history of terrigenous sedimentation provides insight into sea–land interaction in the near-continental regions of the World Ocean during the dramatic last deglaciation period of continental glacial sheets and related glacioeustatic transgression. The submarine Shirshov Ridge located in the Bering Sea deep-water basin is a unique object for the study of peculiar background hemipelagic sedimentation and ice rafting, because terrigenous sedimentation on it is geomorphologically isolated from the intense near-bottom sedimentary fluxes descending along continental slopes.

Terrigenous flux is supplied to the Bering Sea mainly with river runoff and, to a lesser extent, with coastal abrasion (Lisitzin, 1959) and eolian transfer (Serno et al., 2014). Its further distribution is controlled by sea ice and algal rafting (Lisitzin, 1959, 2002) and transportation with water masses as suspended matter supplying from the river mouths (Wang et al., 2016). Since all large rivers discharge terrigenous flux on the spacious northern shelf of the Bering Sea (Fig. 1), the field of terrigenous suspended matter above the deep-water basin and Shirshov Ridge is formed by the residual finely dispersed mixture of several large rivers, which remained after the selective precipitation of significant fraction of sedimentary material during its transportation through the shelf
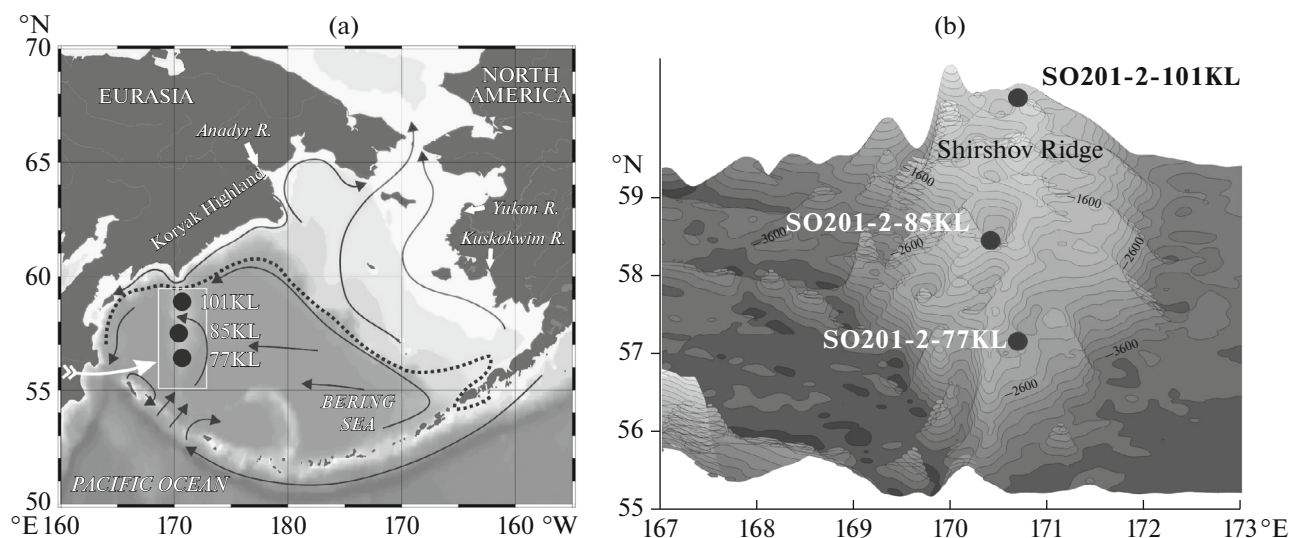
Fig. 1. Map of the Bering Sea and position of the studied cores (a). Magnified bathymetric map of the Shirshov Ridge according to ETOPO1 database with a resolution of 1 min (Amante and Eakins, 2009) indicating the position of mentioned stations (b). Black arrows show the direction of surface currents, white arrow shows the propagation of volcanic material, and dashed line denotes the modern boundary of sea ice distribution according to (Zhang et al., 2010).

(Lisitzin, 1959, 1966; Murdmaa, 1987). Residual suspended matter is subdivided behind the shelf margin into the surface and bottom fluxes (Alekseeva et al., 2015). The bottom flux is spread over abyssal plain of the deep-water sea basin, while the surface flux forms a background reserve of terrigenous suspended matter in the top layers of water column. Only this surficial lateral suspended flux provides hemipelagic terrigenous sedimentation on seamounts, including the Shirshov Ridge. Input of the superdistal eolian dust mainly from the arid zone of the central and eastern Asia (Serno et al., 2014) under the subpolar humid conditions is negligible as compared to the fluvial terrigenous input (Lisitzin, 2002).

The source areas of the Bering Sea were studied by means of mineralogical analysis of the modern sediment (Lisitzin, 1959, 2002; Nechaev et al., 1994), clay minerals (Naidu et al., 1995; Levitan et al., 2013; Alekseeva et al., 2015; Wang et al., 2016), and isotope and geochemical analyses of eolian dust in the northwestern Pacific and its traces in the surface sediment layer (Asahara et al., 2012; Serno et al., 2014).

Only a few data are available on the sedimentation evolution in the Bering Sea during glacial–interglacial cycles. The grain-size and mineral variability of bulk sediment during two last glacial–interglacial cycles was studied in (Levitan et al., 2013; Alekseeva et al., 2015). Variations of bottom current velocities within this time interval were estimated for the first time in (Levitan et al., 2013).

The aim of this work is to reconstruct history of terrigenous sedimentations on the Shirshov Ridge in the western Bering Sea during the last deglaciation (Termination I), i.e., during a gradual transition from the

Last Glacial Maximum to the modern interglacial stage. Mechanisms of terrigenous sedimentation and variability of the bottom current velocities were deciphered on the basis of uninterrupted grain-size distributions (GD) of bulk sediment and its terrigenous component using the statistic method of end-member (EM) modeling (Weltje, 1997; Weltje and Prins, 2003; Prins et al., 2002; Hamann et al., 2008; Jmker et al., 2012; and others), and calculation of the average diameter of sortable silt ($\overline{SS}$) (McCave et al., 1995; McCave and Hall, 2006). The comparison of GD for samples of bulk sediment and their terrigenous component showed that the removal of biogenic components virtually does not affect the proportions of grain-size fractions. Hence, the sections of both the cores within the considered time interval are mainly represented by terrigenous sediments of different grain-size types, with subordinate biogenic admixture.

The studied sections contain two volcanic ash layers, which are considered separately from terrigenous sedimentation, whereas ash admixture in terrigenous sediments is ascribed to the volcanogenic–terrigenous components. Paleosettings were reconstructed using the published age model (Max et al., 2012) for six time intervals: Last Glacial Maximum (22–20 ka), early deglaciation (20–17.5 ka), Heinrich 1 event (17.5–14.8 ka), Bølling–Allerød (14.8–12.9 ka), Younger Dryas (12.9–11.6 ka), and early Holocene (11.6–9.2 ka).

MODERN PHYSICAL–GEOGRAPHICAL AND OCEANOLOGICAL CONDITIONS

The Bering Sea is located in the northern subpolar Pacific. It is connected through the shallow-water

(~50 m) Bering Strait with the Arctic Ocean in the north, and is bordered by the Commander–Aleutian island arc in the south (Fig. 1). The northern and northeastern parts of the basin are occupied by a spacious shelf, whereas the central and western parts represent a deep-water basin with flat floor and maximum depth of 4151 m, which comprises the aseismic Shirshov and Bowers ridges.

Surface waters are involved in a cyclonic circulation beginning in the southern Bering Sea, where the surface waters of the northern Pacific flow into the basin area through the straits of the Commander–Aleutian island arc (Arsen'ev, 1967). Then, the surface waters follow along the continental slope surrounding the deep-water basin of the Bering Sea and return into the open Pacific through the Kamchatka Strait.

The vertical structure of the water column consists of four water masses: surface water manifested only in summer (from 0 to 25−50 m), intermediate Bering Sea (from 25−50 to 100−150 m), intermediate Pacific (150−800 m), and deep-waters (>800 m) (Luchin et al., 1999). At present, water mass located below 800 m is supplied from the open Pacific and represents a mixing product between the North Atlantic Deep Water, Circumpolar Deep Water, and Antarctic Intermediate water. This water is characterized by high nutrient concentrations and has a homogenous structure. Thus, core sampling locality at present is washed by the same water mass. The oxygen minimum zone is developed at depths of 500−1700 m, reaching maximum at 900−1000 m (*WOA*, 2009).

At present, seasonal fast ice is formed in the northern and northeastern parts of the coastal zones (Niebauer et al., 1999). At the coastal shoal, sea is frozen to the bottom. As a result, ice is loaded with bottom sediments, which represent the main constituent of ice-rafted material. This ice begins to form in November and reaches maximum development in March. Tides leading to the 1.5−2 m sealevel rise, on average, with a rate of 1−2 m/s in the northern part play an important role in the ice loading with bottom sediments (Lisitzin, 2002). Sea surface above the deep-water basin remains free of ice during the entire year.

The atmospheric circulation is related to the position of the centers of atmospheric pressure: Aleutian Low and winter Siberian High. The eastward displacement of the Aleutian Low facilitates the development of cold winds above the Bering Sea, which provides intense sea ice formation in the coastal ice holes and abundant southward propagation of pack ice (Cavalieri and Parkinson, 1987). With westward displacement of the Aleutian Low, the wind direction changes to south, while warm flows retard its propagation in the deep-water basin (Cavalieri and Parkinson, 1987).

Among rivers entering into the Bering Sea, the largest sources of terrigenous flux are the Yukon, Kuskokwim, and Anadyr rivers. The Yukon River supplies 68×10^6 t/yr of the terrigenous material (Lisitzin,

2002). The Yukon and Kuskokwim water drainage basins in Alaska are made up of Paleozoic and Mesozoic metamorphosed sedimentary and volcanic rocks (Beikman, 1980). The Anadyr River drains mainly Cretaceous−Tertiary volcanic rocks and granitoids of Chukotka (Zonenshain et al., 1990).

Numerous active volcanoes of Kamchatka and the Aleutian islands during explosive eruptions supply ash material in the northern Pacific, which can be propagated with air for over 1000 km from the eruption center.

MATERIALS AND METHODS

To solve the set problems, we analyzed samples taken from cores SO201-2-85KL (57°30.30′ N, 170°24.79′ E, depth 968 m) and SO201-2-77KL (56°19.90′ N, 170°41.97′ E, depth 2163 m) recovered from the Shirshov Ridge during Cruise of R/V *Zonne* in 2009 (*SO201-KALMAR* ..., 2009). Preliminary description of core sections was carried out on the basis of visual observation and given in the same report (Fig. 2). Analyzed samples were collected on-board and freeze-dried.

Age models of the cores for the deglacial interval are based on the regional correlation of curves of the relative calcium content determined by the X-ray fluorescence. Age of the top of the cores was confirmed by the AMS ^{14}C radiocarbon dates (Max et al., 2012).

Grain-size analysis. The grain-size analyses were carried out on a SALD-2300 laser diffraction particle size analyzer (Shimadzu, Japan) in the Laboratory of the Atlantic Geology of the Atlantic Branch of the Shirshov Institute of Oceanology, Russian Academy of Sciences. The main advantage of the laser analysis is obtaining uninterrupted functions of the grain-size distribution (GD). Each sample was analyzed twice: for bulk sediment after the removal of organic matter by H_2O_2 and for its terrigenous component after the subsequent removal of organic matter by H_2O_2, carbonates by HCl, and biogenic silica by sodium hydroxide (Fig. 3). During sample preparation, particles were disintegrated using sodium tripolyphosphate and ultrasound bath.

The grain-size fractions were extracted following the modified scale (Wentworth, 1922), with boundaries between sand and silt and between silt and clay taken at 63 and 2 μm, respectively (Friedman and Sanders, 1978). The average size of silt particles sorted by bottom currents (terrigenous fraction of 10−63 mm or "sortable silt" $\overline{SS}$) was used as an indicator of paleocurrent intensity (McCave et al., 1995; McCave and Hall, 2006). Elevated values of this parameter indicate an increase of relative velocity of paleocurrents.

Statistic parameters of the grain-size distribution ($\overline{SS}$, average, sorting) were calculated using the GRADISTAT software (Blott and Pye, 2001).
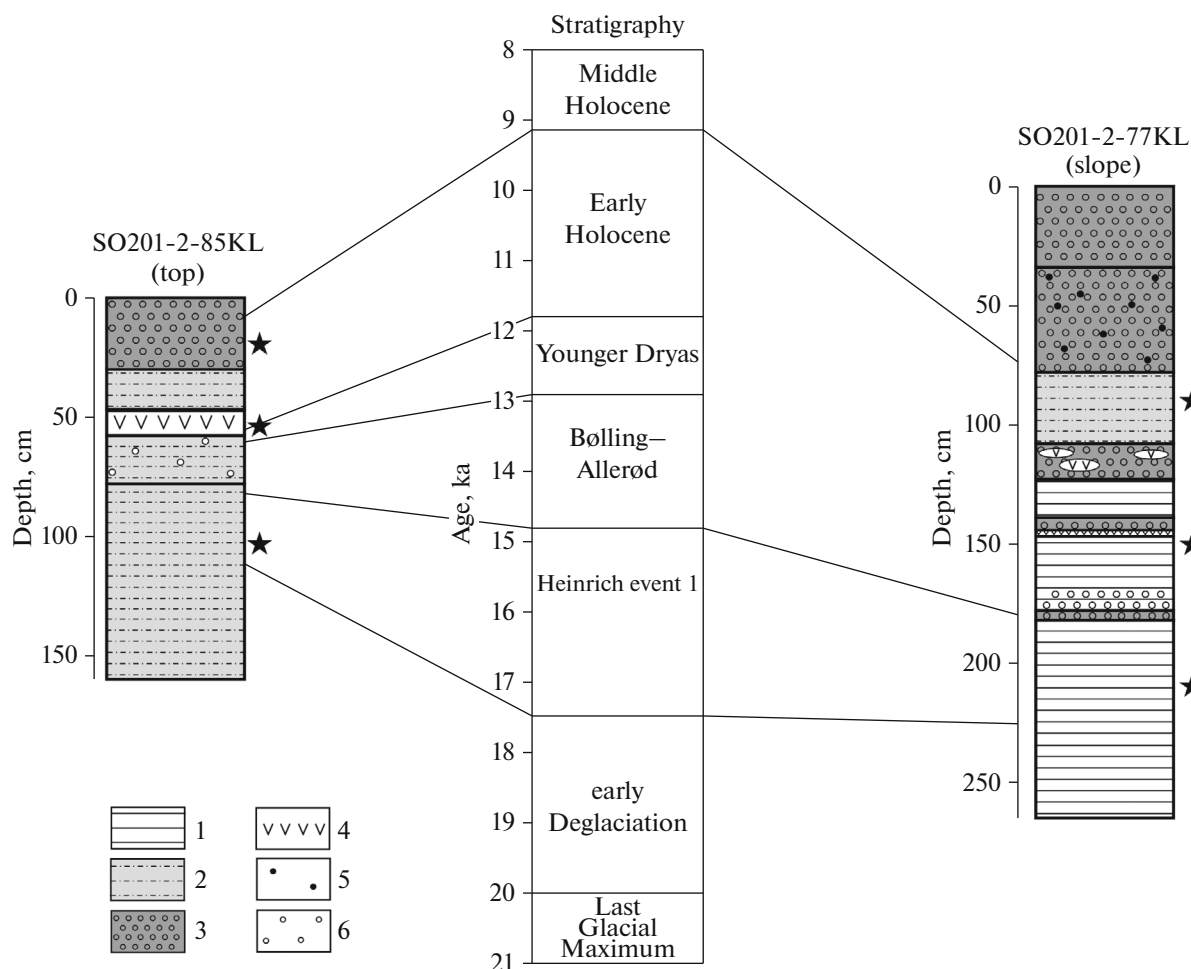
Fig. 2. Lithology and stratigraphy of cores SO201-2-85KL and SO201-2-77KL. Lithology is modified after (*SO201-KALMAR* ..., 2009); age model, after (Max et al., 2012). Asterisks show the position of samples collected for the mineralogical analysis. (1) Sand−silt−clay ooze; (2) sand−clay silt; (3) diatom ooze; (4) volcanic ash; (5) terrigenous admixture; (6) diatoms.

End-member modeling was applied to distinguish the modal fractions of GD, which reflect the main sources of sedimentary material and processes of sediment transportation. The method consists in unmixing the initial function into end members (subpopulations) and determination of the contribution of calculated functions in each GD. This method is widely applied for the genetic interpretation of data of a detailed grain-size analysis (Weltje, 1997; Weltje and Prins, 2003; Prins et al., 2002; Hamann et al., 2008; Jmker et al., 2012; and others).

To divide the polymodal GD of sediment into genetically related particle subpopulations, we applied the non-parametric EM modeling. Calculations were made for all samples, except for samples from the intervals of 47−57 cm from core SO201-2-85KL and 109−122 cm from core SO201-2-77KL, which correspond to the volcanic ash interlayers strongly disturbed during the core extraction from pipe (*SO201-KALMAR* ..., 2009; Ponomareva et al., 2013). Data were processed using AnalySize 1.1.2 which is Matlab based software (Paterson and Heslop, 2015). Correlation between the calculated (model) EMs and the initial GD is shown in Fig. 4a. The observed GD are best described by three EMs (Fig. 4b).

X-ray phase analysis. The mineral composition of samples was analyzed using the X-ray powder diffraction in the Analytical Laboratory of the Institute of Oceanology of the Russian Academy of Sciences on an X-ray diffractometer D8 ADVANCE (Bruker AXC), with Cu-Kα, Ni 0.02 filter, 40 kV, 40 mA, and a LYNXEYE strip detector. Data were collected by scanning in a discrete regime with a step size of 0.02, counting time of 8 s per step, in the range of 2.5−70°2Θ with rotation. The obtained XRD data were processed and deciphered using DIFFRAC.EVA software. Corundum numbers from the ICDD database were used for the quantitative analysis.

Three samples were taken from each core for the X-ray mineralogical analysis to characterize the lithologically and climatically contrasting intervals (Fig. 2).
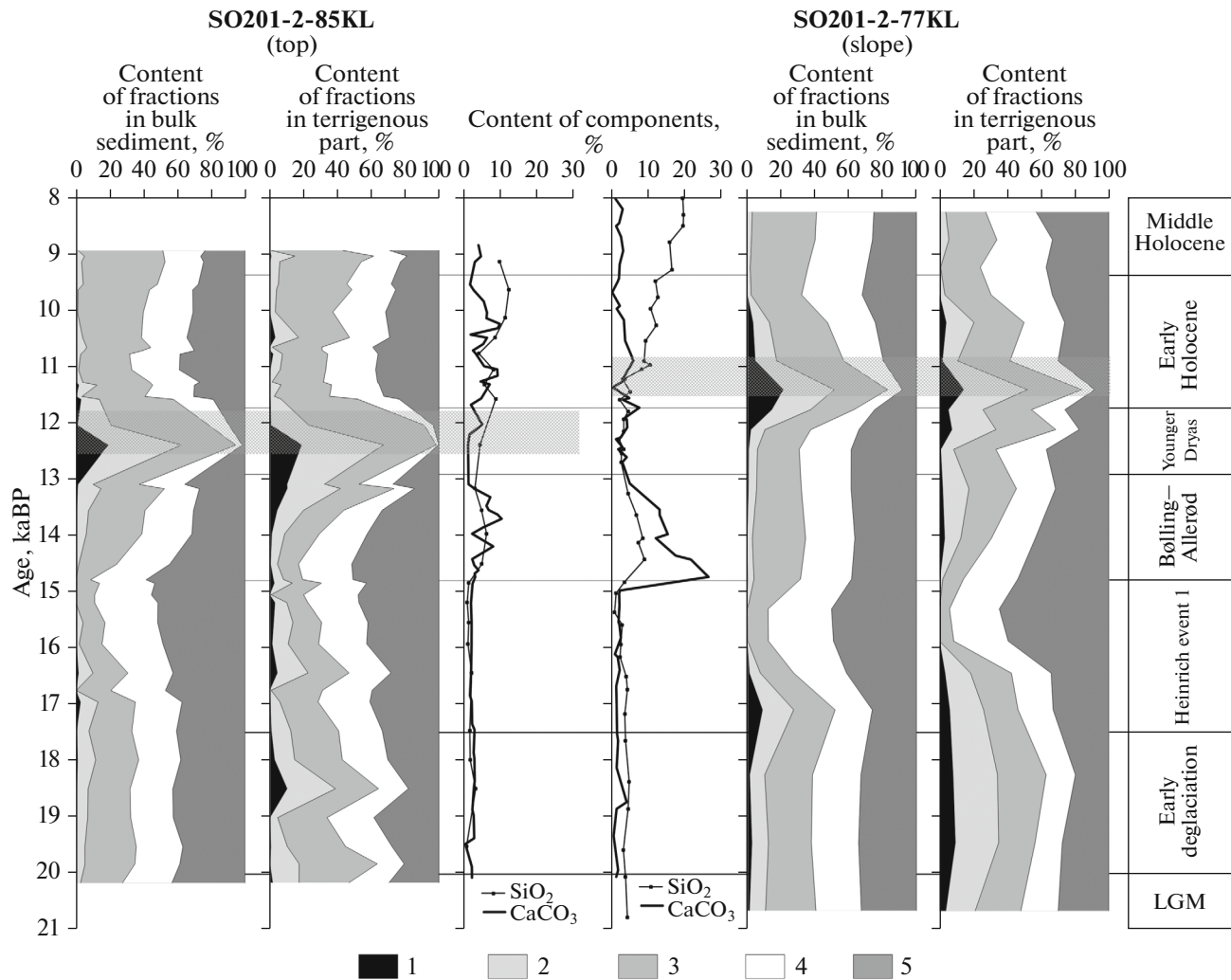
Fig. 3. Comparison of the grain-size composition of bulk sediment and its terrigenous part. Contents of CaCO$_3$ and SiO$_2$ are given after (Riethdord et al., 2013) Gray boxes distinguish intervals of the volcanic ash after (*SO201-KALMAR ...*, 2009). Size fractions: (1) >125 μm, (2) 63−125 μm, (3) 10−63 μm, (4) 2−10 μm, (5) <2 μm.

The lower samples in each core characterize sediments of Heinrich 1 event. The middle samples were taken from sediments of cold Late Dryas in core SO201-2-77KL and from volcanic ash layer of the same age in core SO201-2-85KL. Upper samples are ascribed to the Early Holocene in both cores.

RESULTS

Grain-size composition of bulk sediment and its terrigenous component. Bulk sediment from core SO201-2-85KL is mainly made up of clay (<2 μm) and silt (2−63 μm) particles (Fig. 3). The content of clay fraction gently decreases from 36−58% in the lower part of the core to 23−38% in its upper part, averaging 35.6%. Minimum contents of the clay fraction 1.7−19% are observed within the interval of 47−57 cm, which corresponds to the volcanic ash layer (*SO201-KALMAR ...*, 2009) in Late Dryas.

The silt content in general is constant, averaging 57%. The contribution of sand fraction (>63 μm) is insignificant, with the average sand content of 5.3%. However, within an interval of 47−57 cm consisting of the deformed volcanic ash layer (12.4 ka), the sand content reaches 62.3% (Fig. 3).

After the removal of biogenic components (CaCO$_3$ and biogenic opal-a), the proportions of clay, silt, and sand in the sediment have been changed. In particular, the content of clay fraction in core 85KL decreased and accounted for on average 31.8%. The silt content also decreased, averaging 55.3%. This was accompanied by the simultaneous increase of sand fractions up to 20−38% within intervals of 101−102, 121−122, and 134−137 cm, which correspond to the Heinrich 1 event and the early deglaciation.

In samples of bulk sediment in core SO201-2-77KL, the content of clay fraction is virtually constant
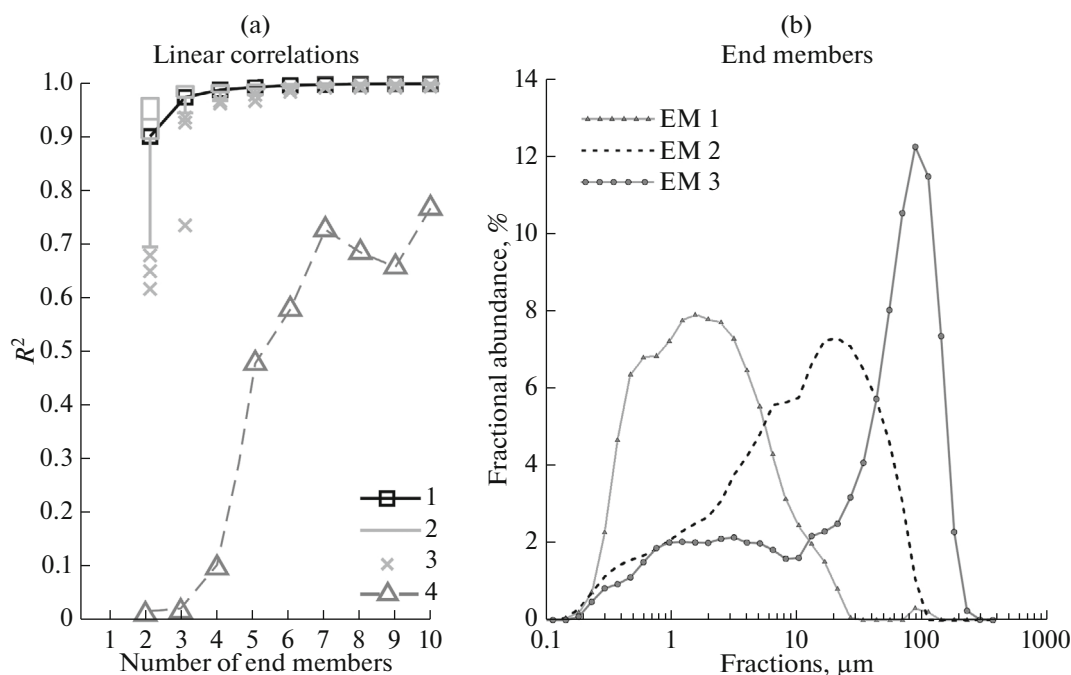
(a)
Linear correlations

(b)
End members

Fig. 4. Results of end member (EM) modeling for the grain-size data obtained for sediments from cores 85KL and 77KL. (a) Degree of correspondence between the number of obtained EMs and initial data. (1) Correlation between the observed grain-size distributions (GD) and calculated EMs for the whole data set; (2) box-plot of correlations between the amount of modeled EMs and individual GD; (3) individual GD falling beyond the 95% confidence interval, (4) correlation between EMs. (R^2) Determination coefficient. (b) Grain-size distribution of calculated EMs.

and on average accounts for 32%, which is slightly lower than that in core SO201-2-85KL. The silt content is similar to that in core SO201-2-85KL, averaging 56.6%. The content of sand fraction in core SO201-2-85KL is slightly higher, averaging 11.4% in the bulk sediment. Maximum contents of the sand fraction (27 and 51%) were found in intervals 121−122 cm and 221−222 cm, which correspond to ash layers at the Younger Dryas−Early Holocene boundary and the middle Heinrich 1 event, respectively. The maximum content of sand fraction (17%) in sample 121−22 cm is ascribed to the volcanic ash layer (Ponomareva et al., 2013).

The content of clay fraction in the terrigenous component of core SO201-2-77KL is slightly higher as compared to that of bulk sediment (on average, 34.4%). The silt content after the removal of biogenic component decreased and accounted for on average 49.1% owing to increase of the sand fraction (up to 16.5%, on average).

The terrigenous component of the sediment shows the unimodal and bimodal GD. Results of the EM modeling over all terrigenous GD, in addition to volcanic ash layers, are shown in Fig. 4. The determination coefficient (R^2) of the measured and calculated data shows that GD for both these cores are best approximated by three EM functions. This gives the high linear correlation of measured and calculated data ($R^2 = 0.97$) and low correlation between calculated EMs ($R^2 = 0.008$) (Fig. 4a). Both these conditions are

necessary for the successful approximation of observed data (see for instance (Paterson and Heslop, 2015)). GD of three calculated EMs are shown in Fig. 4b.

Mineral composition of sediments. In spite of the diversity of rocks that compose the continental surrounding of the Bering Sea, including drainage basins of three largest rivers (Beikman, 1980; Zonenshain et al., 1990), the complex of major rock-forming minerals identified in the bottom sediments by the XRD method is sufficiently uniform (Table 1). Exception is sample (56−57 cm) collected from a volcanic ash layer (47−57 cm) in core SO201-2-85KL. This sample contains anorthite (62%) in association with orthoclase (7%) uncommon for the pyroclastic material, quartz (6%), and trace magnesian calcite, which likely was entrapped in sample from the host sediment. The terrigenous component from other five samples contains the following minerals: quartz (16−25%), albite (16−24%), microcline (6−9%), hornblende (3−5%), and clinopyroxenes represented by diopside and augite (3−4%). Most samples contain dolomite (up to 1%).

Proportions of four major terrigenous clay minerals were determined in the unoriented powder specimens. The clay fraction in all studied samples is characterized by the chlorite−illite assemblage with the subordinate smectite and kaolinite (Fig. 5). The clay minerals account for 34−38%. However, interval of 151−152 cm from core SO201-2-77KL with the highest content of

Table 1. Mineral composition of bottom sediments in the western part of the Bering Sea based on the X-ray diffraction phase analysis

Mineral	Core no., sample					
	SO201-2-77KL			SO201-2-85KL		
	91—92 cm	151—152 cm	211—212 cm	20—21 cm	56—57 cm	101—102 cm
Quartz	22	16	17	16	6	25
Albite	24	16	21	19		20
Anorthite					62	
Microcline	6	6	9	8		8
Orthoclase					7	
Amphibole	3	5	5	5		4
Pyroxene	4	3	4	4		3
Calcite	5	2	2	7	5	3
Mg-calcite					1	
Dolomite		1	1	1		1
Smectite	6	5	6	6	3	5
Illite	13	30	15	14	6	14
Kaolinite	5	5	5	5	2	5
Chlorite	10	10	12	10	3	10
Gypsum	1	1	3		2	1
Bassanite		Traces		2		
Pyrite				3	3	

clay minerals (about 50%) differs in the extremely high illite content (about 30% wt %).

Association of clay minerals has uniform composition and includes the dioctahedral smectite, trioctahedral Fe—Mn chlorite, illite with low content of smectite layers, and kaolinite.

Mixed-layer phases were found in trace amounts only in the volcanic ash layers: in sample 211—212 cm from core SO201-2-77KL and in sample 56—57 cm from core SO201-2-85KL.

Calcite (2—7%) in bulk sediments is related to the calcareous biogenic remains: foraminiferal tests and coccoliths. Pyrite (up to 3%) obviously of diagenetic origin was found in two upper samples from core SO201-2-85KL.

DISCUSSION

The grain-size and mineral composition of terrigenous component of the studied postglacial sediments of the Shirshov Ridge was formed by the mixing of terrigenous material supplied from different source areas of the surrounding land. Quantitative proportions of three end members distinguished from the grain-size distributions (Fig. 6) provide insight into the relative contribution of two major mechanisms of transport and sedimentation (hemipelagic sedimentation and sea ice rafting), as well as the influence of bottom currents.

The mineral composition of postglacial terrigenous sediments covering the ridge was formed by the mixing of material supplied from different distal source areas.

Sources and transport pathways of the terrigenous material. As shown by previous studies (Lisitzin, 1959, 1966, 2002; Wang et al., 2016), the main part of terrigenous material from sand to the finest (submicron) clay particles were supplied during the entire considered time range (about 20—22 ka) by the large Yukon, Kuskokwim, and Anadyr rivers.

At present, under the Holocene interglacial highstand conditions, these rivers discharge terrigenous flux on the spacious shelf, where waves and currents cause the primary differentiation of river sediments into the relatively coarse-grained (mainly sand) and fine-grained (silt—clay) fractions. Sand (63—2000 μm) is supplied to the sea floor and sorted by grain size mainly in the zone of active wave action (down to depths of about 30—50 m). The finely dispersed silt—clay material is retained for some time in the suspended state in the form of near-mouth plumes studied in detail, for instance, on the northeastern coast of the Black Sea (Zavialov et al., 2014). Owing to the mixing of freshened waters of these plumes with seawater, suspension descents on the floor, thus forming the high-density bottom flows on the outer shelf. These flows located
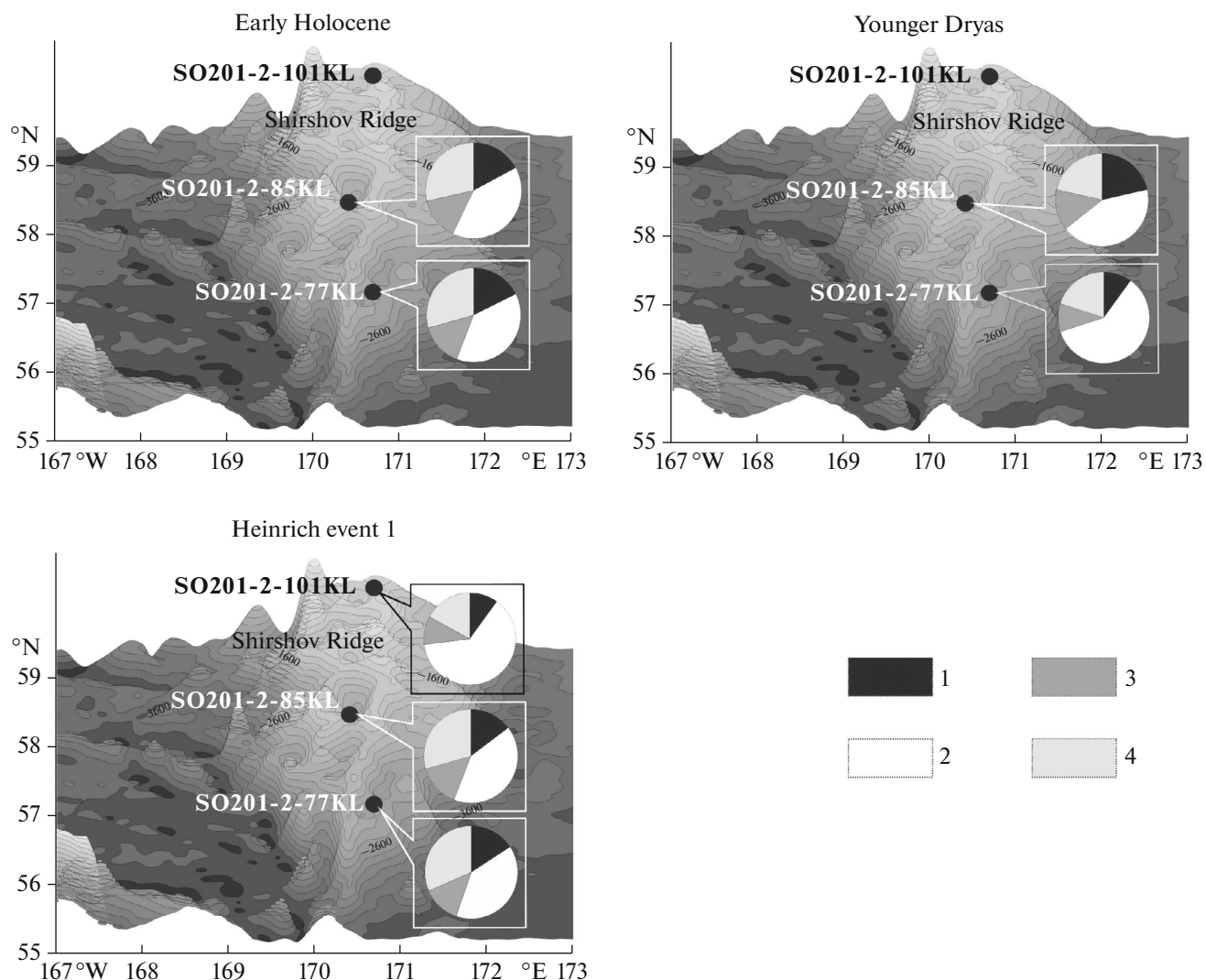
Fig. 5. Content of clay minerals in the postglacial sediments of cores SO201-2-101KL (Levitan et al., 2013), SO201-2-85KL, and SO201-2-77KL. (1) Smectite, (2) illite, (3) kaolinite, (4) chlorite.

beneath the lighter "pure" water succession behave as a "heavy liquid" able to flow down along the canyons of continental slope under gravity (Yakubenko, 2011; Esin et al., 2018). This bottom suspension layer supplies the fine-grained sediments of the outer shelf. Only a small fraction of river particulates supplements the background reserve of the suspended matter of the upper layers of water column. In spite of significant differences of the Bering Sea from the Black Sea and much wider shelf of the former, this mechanism of the distribution of solid load of rivers also operates under highstand conditions.

A different setting occurred during last glacials and related global lowstand, when the shelf represented the coastal plain, while rivers were discharged directly on the continental slope. In addition to the sharp decrease of erosion basis and the erosion of loose sediments of the former shelf, this should lead to the sig-

nificant increase of terrigenous flux, including suspended matter, into the deep-water basin. This would result in the increase of hemipelagic sedimentation rate on the Shirshov Ridge and the coarsening of hemipelagic sediments accumulated there. However, such trends are not observed (Figs. 3, 7). One may suggest that the majority of river runoffs under such extreme conditions were transferred by gravity flows of different type downward the continental slope on the floor of the deep-water basin, and volumetric variations of the supplied sedimentary material did not control significantly the hemipelagic sedimentation on the Shirshov Ridge. Such hypothesis requires additional verification.

The sea ice rafting concept developed for the first time by the example of the Bering Sea (Lisitzin, 1959) mainly concerns the coarse-grained material, i.e., rock fragments more than 2 mm. The studied cores
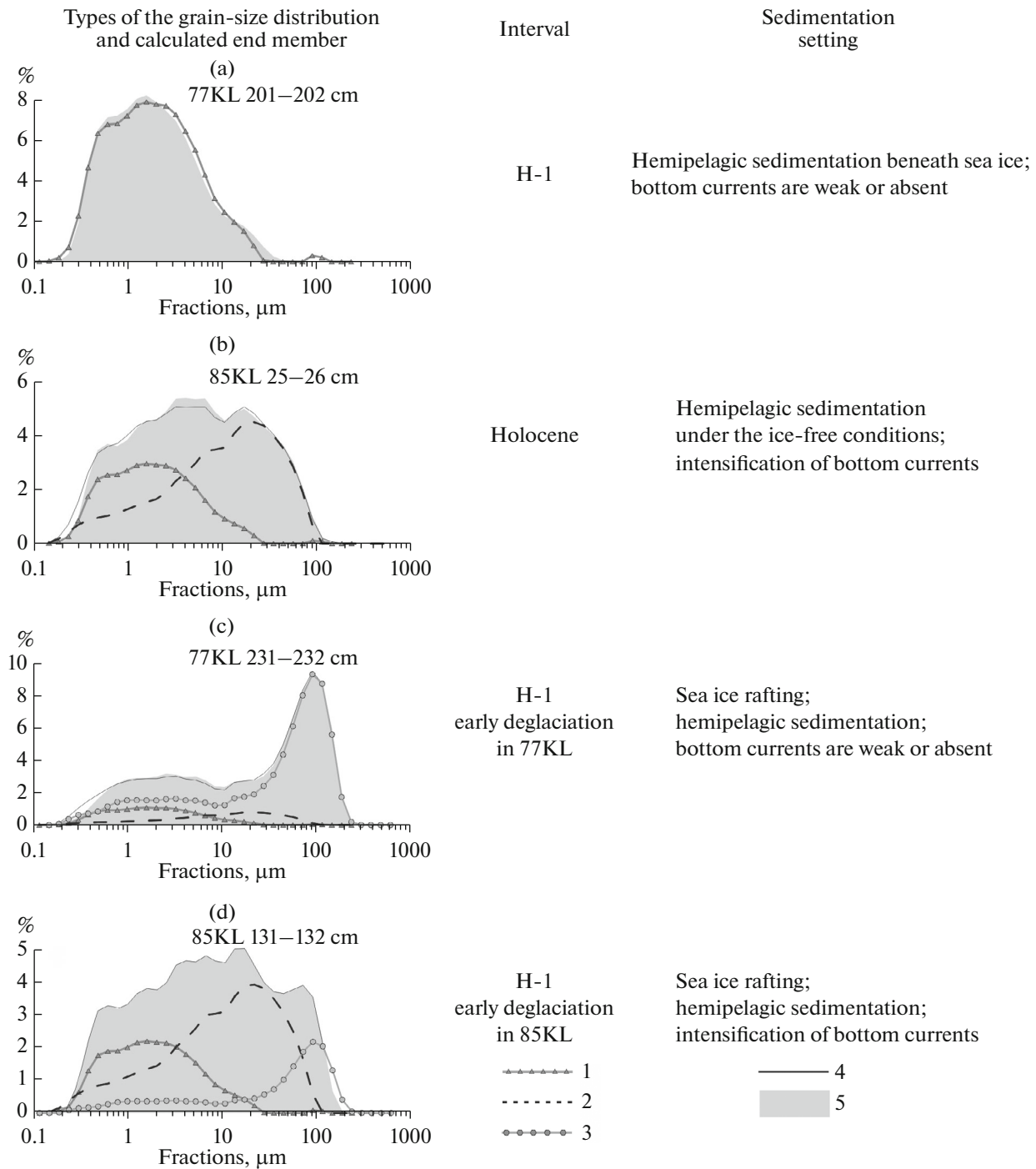
Types of the grain-size distribution
and calculated end member

Interval

Sedimentation
setting

(a)
77KL 201−202 cm

H-1

Hemipelagic sedimentation beneath sea ice;
bottom currents are weak or absent

(b)
85KL 25−26 cm

Holocene

Hemipelagic sedimentation
under the ice-free conditions;
intensification of bottom currents

(c)
77KL 231−232 cm

H-1
early deglaciation
in 77KL

Sea ice rafting;
hemipelagic sedimentation;
bottom currents are weak or absent

(d)
85KL 131−132 cm

H-1
early deglaciation
in 85KL

Sea ice rafting;
hemipelagic sedimentation;
intensification of bottom currents

1 2 3 4 5

Fig. 6. Main types of the grain-size distribution (GD) in the terrigenous component of sediment with addition of the end members (EM) distribution, stratigraphic assignment of samples, and interpretation. (1) EM-1, (2) EM-2, (3) EM-3, (4) summary approximating function, (5) initial GD.

contain only rare gravel-size grains, while larger fragments are absent. Sea ice rafting explains the presence of significant amount of sand and some coarse silt on the Shirshov Ridge, which cannot be transferred as suspended matter for large distance.

Sea ice rafting of terrigenous material is mainly controlled by the drifting fast ice, which is most intensely loaded with sediments on the coastal shoal frozen to bottom (Niebauer et al., 1999). Suspended matter frozen into open-sea ice is of much lesser sig-
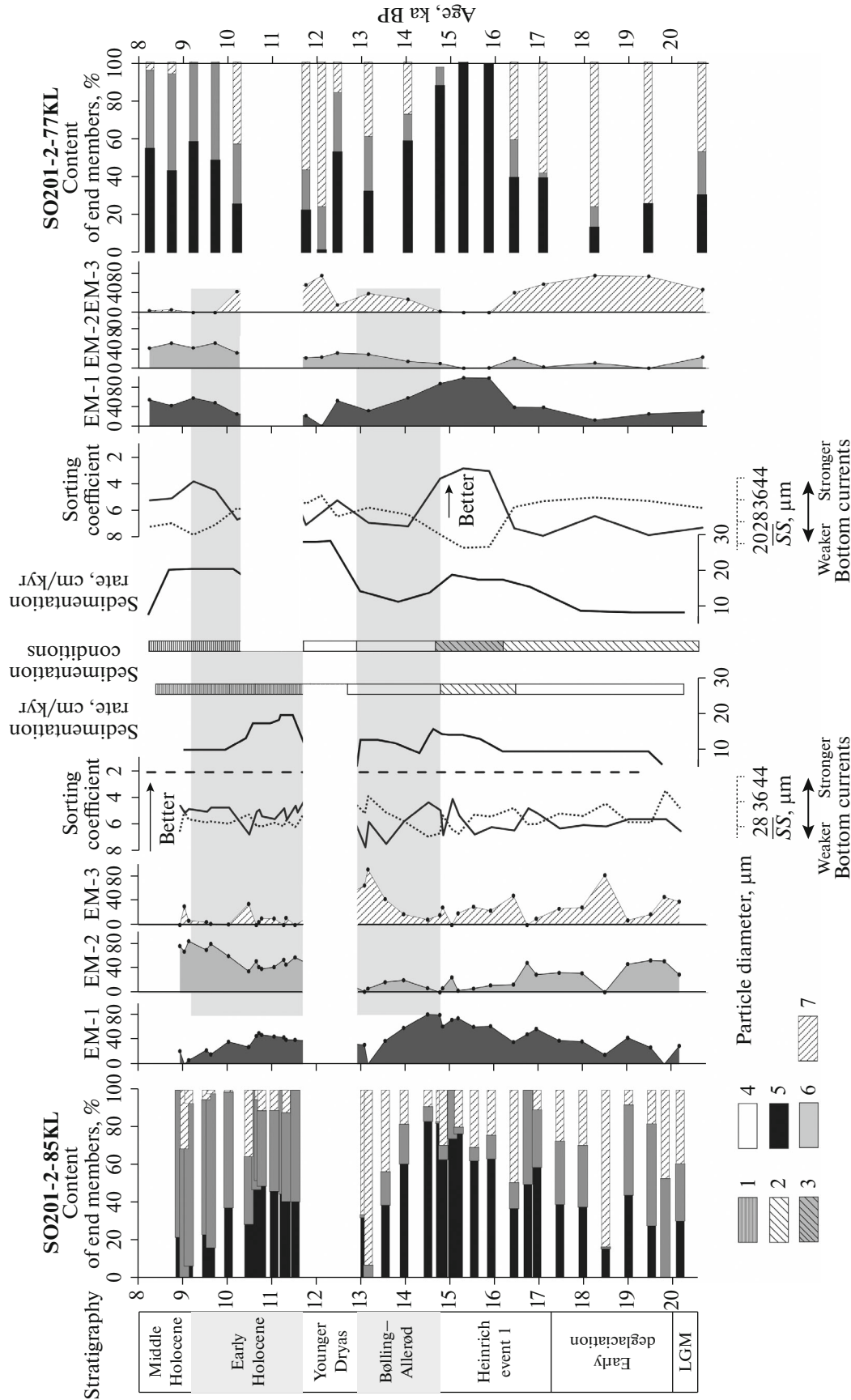
Fig. 7. Results of the grain-size analysis, statistic treatment, and interpretation of terrigenous sedimentation settings on the Shirshov Ridge for an interval of last 22 ka. $\overline{SS}$ is sortable silt (10—63 μm); (1) hemipelagic sedimentation under ice-free conditions, (2) hemipelagic sedimentation, sea ice-rafting, bottom currents are weak or absent; (3) hemipelagic sedimentation under conditions of drifted sea ice and/or permanent sea ice cover, (4) hemipelagic sedimentation, sea ice rafting, intensification of bottom currents, (5) end member EM-1, (6) end member EM-2, (7) end member EM-3. Grain-size data obtained from the volcanic ash interlayers in Younger Dryas (SO201-2-85KL) and Early Holocene (SO201-2-77KL) are excluded from calculations.

nificance. Transport of the drifting sea ice is controlled by the surface water circulation, in our case, by cyclonic circulation above the deep-water basin. The center of circulation represents the main area of seasonal drifting sea ice melting, including fast ice, and, hence, is the main locality for the release and precipitation of ice rafted debris. However, our reconstructions show that during the cold periods of Termination I, dense drifted ice or permanent sea ice cover are accumulated in the circulation center all year. Negative temperatures of surface water prevent sea ice melting and the sea ice rafting is terminated.

The contents of major detrital and clay minerals in postglacial sediments are sufficiently homogenous in both cores and all studied time sections. This fact points to a common averaged terrigenous—mineralogical source area, which reflects the mixing of denudation products of diverse rocks supplied from the surrounding land. Peculiar mineral composition was only found in volcanic ash, which was ejected from the operating Kamchatkan volcanoes during explosive eruptions and has no direct relationship with the terrigenous sedimentation considered in this paper. It is noteworthy that the only analyzed ash sample from a depth of 56—57 cm from core SO201-2-85KL contains minerals atypical of the pyroclastic material, which likely indicates the contamination of the sample by the host terrigenous sediments during core recovery (*SO201-KALMAR ...*, 2009). According to the available literature data, volcanic ash in core SO201-2-77KL is the eruption product of Plosky Volcano located on the Kamchatka Peninsula (Ponomareva et al., 2013).

The predominance of feldspars over quartz, high contents of amphiboles and clinopyroxenes, and the absence of highly resistant accessory minerals of the granite-metamorphic complex allowed us to characterize an integrated source area as "immature" volcanosedimentary province. The quartz—albite association of light minerals and pyroxene—amphibole association of heavy minerals (at high content of chlorite among clay minerals) indicate that the eroded area was made up of mafic volcanic rocks subjected to the low-temperature (greenstone?) metamorphism. Such assumption is confirmed by the finds of epidote in the fine sand fraction (63—100 μm). The chlorite—illite association of clay minerals with low smectite and kaolinite contents suggests the predominant physical weathering in an integrated source area.

Products of the hemipelagic sedimentation and sea ice-rafting are similar in the mineral composition.

This conclusion is consistent with the results of recent studies of modern source areas of the Bering Sea (Wang et al., 2016).

Genetic interpretation of GD and EM. Comparison of the results of grain-size analysis of the bulk sediment and its terrigenous component in cores SO201-2-85KL and SO201-2-77KL showed that the biogenic components of sediment have mainly silt size, i.e., they are mainly represented by the diatom and cocco-lithic remains. Profiles of curves and main trends of the particle distribution in bulk sediment and its terrigenous component remained generally the same after the removal of biogenic components. The grain-size composition of sediment is most affected by the presence of biogenic components in the Bølling—Allerød and Holocene, when surface waters were characterized by the elevated bioproductivity.

Application of the EM modeling allowed us to distinguish genetically meaningful populations of particles. The relative contribution of three EMs into the total GD of two considered cores was used to reconstruct the specifics of terrigenous sedimentation on the Shirshov Ridge during the postglacial time.

The calculated grain-size distribution EM-1 characterizes the contribution of clay and finest silt fraction in the terrigenous sedimentation. The EM-1 mode coincides with 2—3 μm. The fractions were poorly sorted, with sorting coefficient of 3.13. Clay EM-1 reflects the accumulation of sediments during the hemipelagic sedimentation. Source of clay particles (<2 μm) is mainly solid runoff of the Yukon, Kuskokwim, and Anadyr rivers, which is consistent with the grain-size composition of sediments of the Shirshov Ridge determined by other researchers (Levitan et al., 2013; Alekseeva et al., 2015). It is also possible that the clay fraction contains the ice-rafted fine-grained material released from sea ice (Reimnitz et al., 1998). Eolian transfer could also contribute insignificantly to the accumulation of clay fraction (Serno et al., 2014; Wang et al., 2016).

The calculated EM-2 has a mode at 20—30 μm and sorting coefficient of 4.3 (Fig. 4b). The formation of this type of GD was also related to the hemipelagic sedimentation, but was affected by bottom currents. Shift of mode of the calculated grain-size distribution into the sortable silt fraction $(\overline{SS})$ characterizes a selective deposition under the influence of bottom current of moderate intensity.

The calculated EM-3 reflects the influx of sand-size particles, the main source of which on the Shirshov Ridge is the ice-rafted material (Levitan et al., 2013; Alekseeva et al., 2015). Function EM-3 is characterized by the worse sorting (sorting coefficient 5.8). The distribution is bimodal, with the well expressed first mode at 100 μm and the gentle second mode at 1—5 μm. The first clearly expressed mode was likely caused by the load of fast ice with the well-sorted fine-grained sand on the coastal shoal frozen down to the bottom, with its subsequent discharge during sea ice melting above the Shirshov Ridge. The second mode reflects the load of fast sea ice with unsorted mud.

Combination of the calculated EMs in the measured GD of the terrigenous component makes it possible to reconstruct the sedimentation conditions during the last deglaciation (Termination I) in the core sampling locality (Figs. 6, 7). Four GD types formed under different sedimentation conditions are distinguished.

GD of the first type with 100% contribution of EM-1 corresponds to the subice hemipelagic sedimentation of clay and fine-silt material introduced with water masses beneath the ice-covered sea surface at weak or absent bottom currents (Fig. 6a). The low water temperature prevented ice melting and, correspondingly, a supply of the ice-rafted material on the ridge. Such conditions were typical of the second half of the Heinrich 1 event in the southern part of the Shirshov Ridge (core SO201-2-77KL). In core SO201-2-85KL from the middle part of the ridge, only two intervals (84−85 and 104−105 cm) during the Heinrich 1 event contain the ice-rafted material, with insignificant intensification of bottom currents (Fig. 7).

GD of the second type characterized by the increased contents of EM-1 and EM-2 and the absence of EM-3 were formed when the ice-rafted material was not supplied under conditions of ice-free sea existing in the core sampling locality (Fig. 6b). Accumulation of clay−silt hemipelagites of the second type was controlled by bottom currents, which led to the selective deposition of sortable silt particles ($\overline{SS}$) from suspended matter and the formation of well-expressed mode EM-2 at 20−30 μm, according to theoretical considerations by McCave et al. (McCave and Hall, 2006; McCave et al., 2017). This type of sedimentation in the Early and Middle Holocene is observed in both cores. The absence of mode EM-3 excludes the possible formation of silt mode EM-2, which is related to the influx of ice-rafted material. This interpretation is also confirmed by the EM modeling of the grain-size composition of surface sediments in the northern Pacific and Bering Sea (Wang et al., 2016), where the distribution with mode at 30−40 μm corresponds to sediments accumulated by bottom currents. It should be noted that the contribution of EM-2 in core SO201-2-85KL recovered from intermediate depths is higher than that in core SO201-2-77KL within the entire studied interval.

The third type of GD is described by the high content of EM-3 and approximately equal contributions of EM-1 and EM-2, which indicates the contribution of both ice-rafted material and fine-grained fractions owing to the hemipelagic sedimentation (Fig. 6c). Such situation is typical of cold periods of the early deglaciation and the first half of the Heinrich 1 event in core SO201-2-77KL. In core SO201-2-85KL, this setting is observed in the second half of the Heinrich 1 event and during Bølling−Allerød under conditions of increased sedimentation rates of both hemipelagites and ice-rafted material by weak bottom currents.

Increasing influence of bottom currents (elevated contribution of EM-2) during the intense sea ice rafting (great contribution of EM-3) is noted during the early deglaciation in sediments of core SO201-2-85KL, excluding interval 121−122 cm (Fig. 6d). In the Early−Middle Holocene interval, both cores also show signs of the intensification of bottom currents accompanied by a significant decrease of the ice-rafted contribution (Fig. 7). Weakening of bottom currents up to the complete absence of EM-2 is typical of the second half of Heinrich 1 and Bølling−Allerød, which is observed in both cores. On average, the influence of bottom currents is better expressed in sediments of core SO201-2-85KL as compared to core SO201-2-77KL during the entire studied interval, which is likely caused by the shallower sampling depth of the core.

Bottom currents could be intensified by the rearrangement of water mass circulation in relation with opening of the Bering Strait and with climatic changes during deglaciation. According to last data (Jakobsson et al., 2017), the onshore Bering Isthmus was flooded in the Early Holocene 11 ka ago, which could affect the formation of intermediate waters surrounding the slopes of the Shirshov Ridge at core sampling depths. Their more intense formation during drying of the Bering Strait during the Last Glacial Maximum and subsequent deglaciation was assumed in many works, for example, (Max et al., 2014; Knudson and Ravelo, 2015). At the same time, it is known that rates and volumes of the formation of intermediate water mass in the Bering Sea increased during cold events of Heinrich 1 and Younger Dryas owing to the wider distribution of sea ice cover as compared to the modern conditions. According to (Max et al., 2014), the lower boundary of the intermediate water mass descended to a depth of 2 km during at least Heinrich 1. Thus, an intensification of bottom currents reflected in sediments of core SO201-2-85KL (depth 968 m) during the early deglaciation and the first half of the Heinrich 1 event could be related to increasing volumes and rates of the formation of intermediate waters.

However, evidence for weak bottom currents or their absence was found in both cores for the second half of the Heinrich 1 event. This does not confirm the inferred intensification of bottom currents during cold periods. Thus, it remains unclear whether variations in bottom circulation are related to climatic changes, variations of volumes, and rates of the formation of intermediate waters or were caused by some other factors.

An attempt to estimate the current velocity from $\overline{SS}$ (McCave et al., 2017) failed. The fraction of sortable silt entraps the ice-rafted detritus, which increases $\overline{SS}$ values and yields unrealstic large calculated values of bottom current velocities. The assessment of current velocities from $\overline{SS}$ parameter in the ice sedimentation regions remains yet incompletely solved problem.

Sedimentation conditions on the Shirshov Ridge in the postglacial time. Terrigenous sedimentation during the Last Glacial Maximum, early deglaciation, and the first half of the Heinrich 1 event in the southern and central parts of the Shirshov Ridge was caused by a combination of the hemipelagic sedimentation and terrigenous influx with the sea ice (Fig. 7). Bottom

currents at intermediate depths also affected sedimentation.

In the second half of the Heinrich 1 event, only hemipelagic sedimentation is reconstructed for the southern part of the submarine ridge. This is likely related to the accumulation of uninterrupted ice sheet or dense drifting sea ice, whose melting in the core sampling locality was prevented by the low temperature of surface waters. These conditions provided specific subice sedimentation, which was characterized by the absence of pellet mechanism of suspended matter precipitation owing to the low zooplankton production.

During Bølling–Allerød, waters above the Shirshov Ridge were characterized by the high biological productivity and hemipelagic sedimentation controlled by the pellet mechanism. Only separate sea ice plates likely reached the central and southern parts of the Shirshov Ridge, and the influence of sea ice rafting on the terrigenous sedimentation was insignificant.

In the Younger Dryas, the fine suspended matter and the coarser ice-rafted particles were settled from the weakly mobile bottom waters in the southern part of the ridge (Fig. 7).

At the beginning of the Holocene, the southern part of the ridge was dominated by the hemipelagic sedimentation of suspended matter from water column at the absence of sea ice and significant influence of bottom currents. In the central part of the ridge, ice rafting was virtually absent during the entire Holocene, while the terrigenous sedimentation was mainly provided by the hemipelagic precipitation of suspended matter introduced with water masses.

CONCLUSIONS

Peculiarities of terrigenous sedimentation on the Shirshov Ridge during the last deglaciation (Termination I) were reconstructed. Statistical treatment of the grain-size data allowed us to distinguish the main mechanisms of terrigenous influx on the Shirshov Ridge: hemipelagic sedimentation caused by bottom currents of different intensity and supply of ice-rafted material. Their relative role in the terrigenous sedimentation during six stages of Termination 1 was determined. During period from the early deglaciation to the Bølling–Allerød, the terrigenous sedimentation was caused by a combination of hemipelagic sedimentation and sea ice rafting. The probable dense accumulation of drifted sea ice or permanent sea ice cover above the southern part of the ridge in the second half of the Heinrich 1 event caused the subice hemipelagic supply of fine fractions. During the Holocene (modern interglacial), the terrigenous sedimentation was provoked by the hemipelagic precipitation of suspended matter in response to the activation of bottom currents. Such sedimentation setting could exist in local basins, from which the cores were recovered. On the crests of the ridge, the influence of bottom currents was likely much stronger during the entire considered geological interval. This follows from the high content (>50%) of silt fraction (0.01–0.1 mm) in modern sediments of the ridge (Lisitzin et al., 1970, Fig. 74).

Analysis of the mineral composition of sediments showed that the terrigenous material during last 22 ka was supplied on the Shirshov Ridge from the water drainage basins of the Yukon, Kuskokwim, and Anadyr rivers, thus forming a single mixed terrigenous–mineralogical province. In addition, Kamchatka volcanoes during explosive eruptions supplied volcanic ash into the studied area. This ash formed layers and lenses unrelated to the terrigenous sedimentation in both cores.

REFERENCES

Alekseeva, T.N., Murdmaa, I.O., Ivanova, E.V., et al., Sedimentation in the Submarine Shirshov Ridge Area (Bering Sea) during the Last 180–185 ka (Penultimate Glaciation–Holocene), *Lithol. Miner. Resour.*, 2015, no. 5, pp. 341–360.

Amante, C. and Eakins, B.W., ETOPO1 1 arc-minute global relief model: Procedures, data sources and analysis, *NOAA Technical Memorandum NESDIS NGDC-24*, 2009, p. 19.

Arsen'ev, V.S., *Techeniya i vodnye massy Beringova morya* (Currents and Water Masses in the Bering Sea), Moscow: Nauka, 1967.

Asahara, Y., Takeuchi, F., Nagashima, K., et al., Provenance of terrigenous detritus of the surface sediments in the Bering and Chukchi seas as derived from Sr and Nd isotopes: Implications for recent climate change in the Arctic regions, *Deep-Sea Research II*, 2012, vol. 61–64, pp. 155–171.

Beikman, H.M., Geologic Map of Alaska. Scale 1 : 2 500 000, *U.S. Geol. Surv.*, Arlington., 1980.

http://dggs.alaska.gov/webpubs/usgs/un/oversized/beikman_1980_sh-001.pdf

Blott, S. and Pye, K., Gradistat: a grain size distribution and statistics package for the analysis of unconsolidated sediments, *Landforms*, 2001, vol. 26, pp. 1237–1248.

Cavalieri, D.J. and Parkinson, C.L., On the relationship between atmospheric circulation and the fluctuations in the sea ice extents of the Bering and Okhotsk seas, *J. Geophys. Res.*, 1987, vol. 92, no. (7), pp. 7141–7162.

Esin, N.V., Murdmaa, I.O., Esin, N.I., and Evsyukov, Y.D., Dynamics of slow suspension flows on the Black Sea abyssal plain, *Quat. Int.*, 2018, vol. 465, pp. 54–62.

Friedman, G.M. and Sanders, J.E., *Principles of Sedimentology*, New York: Freeman, 1978.

Hamann, Y., Ehrmann, W., Schmiedl, G., et al., Sedimentation processes in the eastern Mediterranean Sea during the Late Glacial and Holocene revealed by end-member

modelling of the terrigenous fraction in marine sediments, *Mar. Geol.*, 2008, vol. 248, pp. 97−114.

Jakobsson, M., Pearce, C., Cronin, T.M., et al., Post-glacial flooding of the Bering Land bridge dated to 11 cal ka BP based on new geophysical and sediment records, *Clim. Past*, 2017, vol. 13, pp. 991−1005.

Jmker, J.I., Stauch, G., Dietze, E., et al., Characterisation of transport processes and sedimentary deposits by statistical end-member mixing analysis of terrestrial sediments in the Donggi Cona Lake catchment, NE Tibetan Plateau, *Sediment. Geol.*, 2012, vol. 281, pp. 166−179.

Knudson, K.P. and Ravelo, A.C., North Pacific Intermediate Water circulation enhanced by the closure of the Bering Strait, *Paleoceanography*, 2015, vol. 30, pp. 1287−1304.

Levitan, M.A., Kuz'mina, T.G., Luksha, V.L., et al., Late Pleistocene Sedimentation History of the Shirshov Ridge, Bering Sea, *Geochem. Int.*, 2013, no. 3, pp. 173−205.

Lisitzin, A.P., *Geographic characteristics of the Bering Sea: Floor morphology and bottom sediments*, *Tr. Inst. Okeanol.*, 1959, vol. 29.

Lisitzin, A.P., *Protsessy sovremennogo osadkoobrazovaniya v Beringovom more* (Processes of Recent Sedimentation in the Bering Sea), Moscow: Nauka, 1966.

Lisitzin, A.P., *Sea Ice and Iceberg Sedimentation in the Ocean: Recent and Past*, Berlin: Springer, 2002.

Lisitzin, A.P., Murdmaa, I.O., Petelin, V.P., and Skornyakova, N.S., Grain size composition of sediments, in *Osadkoobrazovanie v Tikhom okeane* (Sedimentation in the Pacific Ocean), Bezrukov, P.L., Ed., Moscow: Nauka, 1970, pp. 296−323.

Luchin, V.A., Menovshchikov, V.A., Lavrent'ev, V.M., and Khen, G.V., Hydrology of Water, in *Gidrometeorologiya i gidrokhimiya morei* (Hydrometeorolgy and Hydrochemistry of Seas), St. Petersburg: Gidrometeoizdat, 1999, vol. 10, no. 1, pp. 77−153.

Max, L., Riethdorf, J.-R., Tiedemann, R., et al., Sea surface temperature variability and sea ice extend in the subarctic Northwest Pacific during the past 15 000 years, *Paleoceanography*, 2012, vol. 27, p. A3213.

Max, L., Lembke-Jene, L., Riethdorf, J.-R., et al., Pulses of enhanced North Pacific Intermediate Water ventilation from the Okhotsk Sea and Bering Sea during the last deglaciation, *Clim. Past*, 2014, vol. 10, pp. 591−605.

McCave, I.N., Size sorting of fine sediment during transport and deposition: difficulties with mud, *Res. Centre Terramare Rep.*, 2005, vol. 13, pp. 117−119.

McCave, I.N., Formation of sediment waves by turbidity currents and geostrophic flows: A discussion, *Mar. Geol.*, 2017, vol. 390, pp. 89−93.

McCave, I.N. and Hall, I.R., Size sorting in marine muds: Processes, pitfalls, and prospects for paleoflow-speed proxies, *Geochem. Geophys. Geosyst.*, 2006, vol. 7, no. 05, p. Q10.

McCave, I.N., Manighetti, B., and Robinson, S.G., Sortable silt and fine sediment size composition slicing: parameters for paleocurrent speed and paleoceanography, *Paleoceanography*, 1995, vol. 10, pp. 593−610.

Murdmaa, I.O., *Fatsii okeanov* (Facies of Oceans), Moscow: Nauka, 1987.

Naidu, A.S., Han, M.W., Mowatt, T.C., and Wajda, W., Clay minerals as indicators of sources of terrigenous sediments, their transportation and deposition: Bering Basin, Russian-Alaskan Arctic, *Mar. Geol.*, 1995, vol. 127, pp. 87−104.

Nechaev, V.P., Sorochinskaya, A.V., Tsoy, I.B., and Gorbarenko, S.A., Clastic components in Quaternary sediments of the northwest Pacific and their paleo-oceanic significance, *Mar. Geol.*, 1994, vol. 118, pp. 119−137.

Paterson, G.A. and Heslop, D., New methods for unmixing sediment grain size data, *Geochem. Geophys. Geosyst.*, 2015, vol. 16, no. (12), pp. 4494−4506.

Ponomareva, V.V., Portnyagin, M., Derkachev, A., et al., Early Holocene M~6 explosive eruption from Plosky volcanic massif (Kamchatka) and its tephra as a link between terrestrial and marine paleoenvironmental records, *Int. J. Earth Sci.*, 2013, vol. 102, pp. 1673−1699.

Prins, M.A., Bouwer, L.M., Beets, C.J., et al., Ocean circulation and iceberg discharge in the glacial North Atlantic: Inferences from unmixing of sediment size distributions, *Geology*, 2002, vol. 30, pp. 555−558.

Reimnitz, E., McCormick, M., Bischof, J., and Darby, D., Comparing sea-ice sediment load with Beaufort Sea shelf deposits: Is entrainment selective?, *J. Sediment. Res.*, 1998, vol. 68, pp. 777−787.

Riethdorf, J.-R., Nurnberg, D., Max, L., et al., Millennial scale variability of marine productivity and terrigenous matter supply in the western Bering Sea over the past 180 kyr, *Clim. Past*, 2013, vol. 9, no. (3), pp. 1345−1373.

Serno, S., Winckler, G., Anderson, R.F., et al., Eolian dust input to the Subarctic North Pacific, *Earth Planet. Sci. Lett.*, 2014, vol. 387, pp. 252−263.

SO201-KALMAR Leg 2 Cruise Report, Dullo, C., Baranov, B., and van den Bogaard, C., Eds., Kiel: IFM-GEOMAR, 2009.

Wang, R., Biskaborn, B., Ramisch, A., et al., Modern modes of provenance and dispersal of terrigenous sediments in the North Pacific and Bering Sea: implications and perspectives for palaeoenvironmental reconstructions, *Geo-Mar. Lett.*, 2016, vol. 36, no. (4), pp. 259−270.

Weltje, G.J., End-member modelling of compositional data: numerical-statistical algorithms for solving the explicit mixing problem, *Math. Geol.*, 1997, vol. 29, pp. 503−549.

Weltje, G.J. and Prins, M.A., Muddled or mixed? Inferring palaeoclimate from size distributions of deep-sea clastics, *Sediment. Geol.*, 2003, vol. 162, pp. 39−62.

Wentworth, C., A scale of grade and class terms for clastic sediments, *J. Geol.*, 1922, vol. 30, pp. 377−392.

WOA, 2009. World Ocean Atlas. http://www.nodc.noaa.gov/OC5/WOA09/pr_woa09.html

Yakubenko, V.G., Bottom currents on the shelf and continental slope in the northeastern Black Seamoray, in *Kompleksnye issledovaniya Chernogo moray* (Complex Studies of the Black Sea), Esin, N.V. and Lomazov, B.S., Eds., Moscow: Nauchn. Mir, 2011, pp. 68−74.

Zavialov, P.O., Makkaveev, P.N., Konovalov, B.V., et al., Hydrophysical and hydrochemical characteristics of the sea areas adjacent to the estuaries of small rivers of the Russian coast of the Black Sea, *Oceanology,* 2014, vol. 54, no. 3, pp. 265−280.

Zhang, J., Woodgate, R., and Moritz, R., Sea ice response to atmospheric and oceanic forcing in the Bering Sea, *J. Phys. Oceanogr.*, 2010, vol. 40, pp. 1729−1747.

Zonnenshain, L.P., Kuzmin, M.I., and Natapov, L.M., Koryak-Kamchatka foldbelt, in *Geology of the U.S.S.R.: A Plate-Tectonic Synthesis (Geodynamics Ser., 21)*, Page, B.M., Ed., Am. Geophys. Union, Washington, D.C., 1990, pp. 149−167.

Translated by M. Bogina